ASTRO-H

INSTRUMENT CALIBRATION REPORT
DOCUMENT TITLE
ASTH-HXI-CALDB-LSFQE

Version 0.2

DATE Sep 2016

ISAS/ GSFC

Prepared by: Kouichi Hagino

Table of Contents

.

CHANGE RECORD PAGE (1 of 2)

DOCUMENT TITLE : ASTH-HXI-CALDB-LSFQE			
ISSUE	DATE	PAGES AFFECTED	DESCRIPTION
Version 0.1	Nov 2015	All	First release
Version 0.2	Sep 2016	8-12	Second release

.

Introduction

1.1 Purpose

This document describes how the CALDB of line-spread function (LSF) and quantum efficiency (QE) are prepared. The CALDB file structure is define in the ASTH-SCT-04 and available from the Hitomi CALDB web page at http://hitomi.gsfc.nasa.gov.

1.2 Scientific Impact

The HXI response file (RSP) is generated by hxirspeffimg using line spread function/quantum efficiency of HXI and effective area of HXT. To incorporate position dependence of the detector response, quantum efficiency is prepared for each pixel, and both of line spread function and quantum efficiency are divided into 5 layers. The EOB wobbling effect is also corrected with CAMS displacement information. The values of quantum efficiency in QE CALDB include transmission of camera/baffle windows, calibration-source shadow and efficiency of event reconstruction process as well as the probability of photon interactions with detectors.

The LSF/QE CALDB will be updated when Bad/Threshold, Fluorescence Line or Energy Cut CALDB is updated. It is because the detector response depends on the event reconstruction process. Also, accumulation of charge in the detectors affects the detector response.

2 Release CALDB 20151115

Filename	Valid date	Release date	CALDB Versions	Comments
ah_hx1_lsf_20140101v001.fits	2015-01-01	2015-11-15	001	ah_hx1_lsf_20151115v001.fits
ah_hx1_qe_20140101v001.fits	2015-01-01	2015-11-15	001	ah_hx1_qe_20151115v001.fits
ah_hx2_lsf_20140101v001fits	2015-01-01	2015-11-15	001	ah_hx2_lsf_20151115v001fits
ah_hx2_qe_20140101v001.fits	2015-01-01	2015-11-15	001	ah_hx2_qe_20151115v001.fits

2.1 Data Description

The data listed in Table 1 are used for estimation of the noise parameters. These data were taken from low temperature tests performed at ISAS in 2014 December for HXI1 and 2014 October for HXI2. In both experiments, the detectors were irradiated by a radioisotope [241]Am.

.

Table 1. The list of data used to extract noise parameters.

Experimental data of HXI1	Experimental data of HXI2
events_hxi_20141213_021348.root	
events_hxi_20141213_021536.root	events_hxi_20141023_060219.root
events_hxi_20141213_033037.root	events_hxi_20141023_072402.root
events_hxi_20141213_043346.root	events_hxi_20141023_082434.root
events_hxi_20141213_053616.root	events_hxi_20141023_092514.root
events_hxi_20141213_063835.root	events_hxi_20141023_102601.root
events_hxi_20141213_074059.root	

2.2   Data Analysis

Line spread function and quantum efficiency of HXI are generated by Monte Carlo simulation since Compton scattering and secondary emissions are non-negligible in hard X-ray bands. The simulations are performed in following steps:

1. Calculate energy deposits on the detectors by utilizing Monte Carlo simulation for interactions of photons with detectors and passive materials
2. Calculate pulse height from the energy deposits with a simulation of charge transportation in the semiconductor detectors
3. Convolve the pulse height with read-out noise
4. Event reconstruction (algorithm is identical to hxievtid)

This simulation code is based on an integrated response generator "ComptonSoft" (Odaka et al. 2010; https://github.com/odakahirokazu/ComptonSoft).
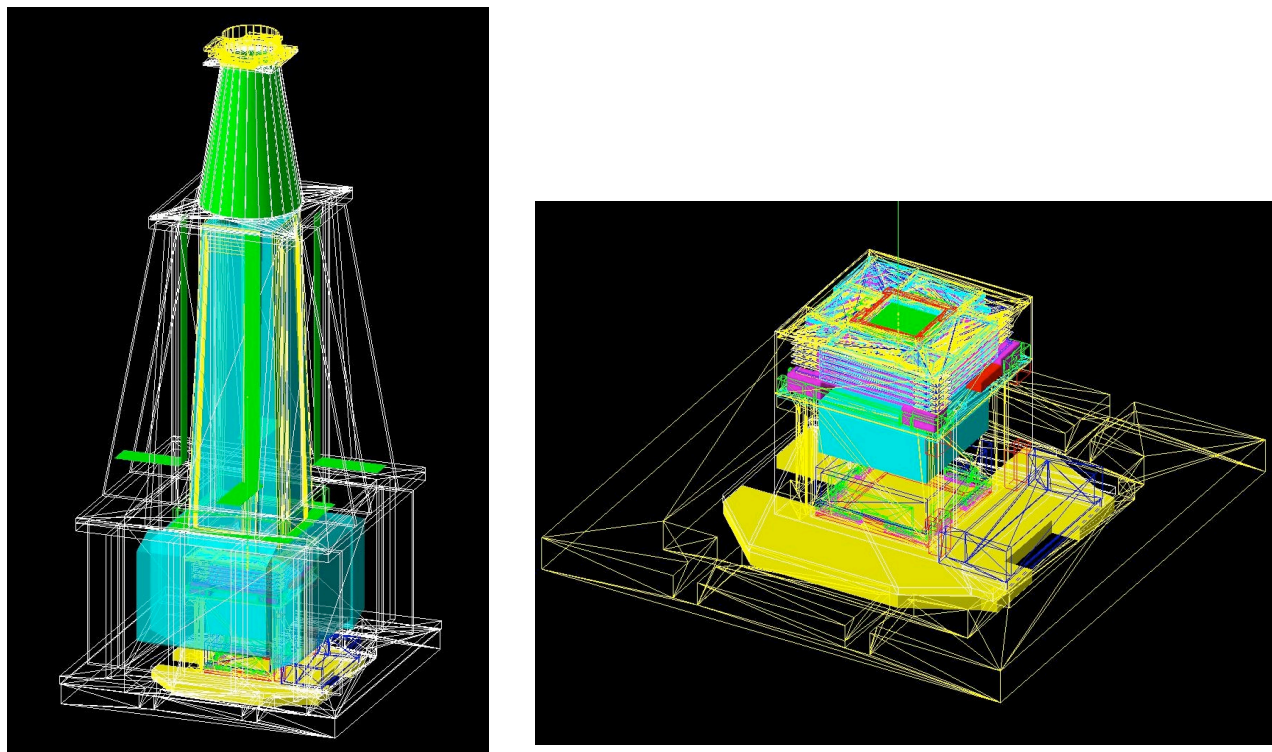

Fig. 1. The mass model of the HXI (left) and the main detector module (right)

.

The Monte Carlo simulation part is based on the Geant4 toolkit library (Agostinelli et al. 2003; Allison et al. 2006), which is widely used for the particle tracking in high-energy physics. Since the detector geometry strongly affects the detector response, a detailed mass model of the HXI is implemented as shown in **Error! Reference source not found.**. Most of the passive materials as well as the main detector module and BGO active shields are included. To generate the line spread function and quantum efficiency, the simulation is performed for each energy bin of line spread function/quantum efficiency with monochromatic photons at the central energy of the energy bin. The photons are generated in a horizontal plane with a size of 32×32 mm^2 located above the entrance window. All the photons have an initial direction to the detector along the optical axis.

In the second step of the simulation, charge loss due to electric field structures and charge trapping are implemented. The former effect is important in Si detectors for HXI because there are thought to exist a positive fixed charge on the surface at gaps between strip electrodes (Takeda et al. 2007). This effect reduces the quantum efficiency at energies below ~10 keV. The latter effect distorts the spectra of CdTe detectors in higher energy bands. This is due to the fact that a mobility-lifetime product of carriers in CdTe is 2-3 orders of magnitude smaller than that of Si.

The noise parameters are obtained from the experimental data. The spectra for each read-out channel were subtracted from the data after the gain correction with the latest gain CALDB. No screening/reconstruction is applied to the data. The line widths of an X-ray line at 59.5 keV from ^{241}Am were obtained by fitting the spectra with Gaussian.

2.3   Results

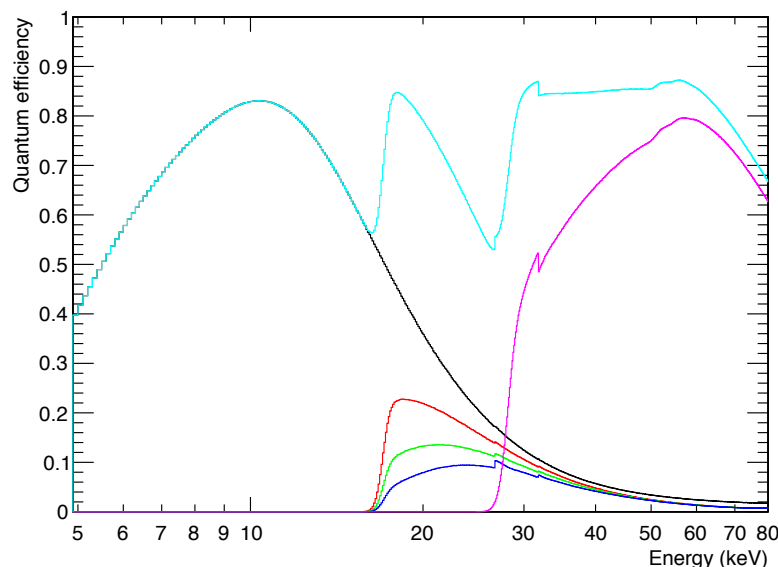**Error! Reference source not found.** shows plots of quantum efficiency averaged for all the

Fig. 2. Quantum efficiencies of HXI2 averaged over all the pixels. Black, red, green, blue and magenta lines represent quantum efficiency for each layer, respectively, while the cyan line is a sum of all layers.

pixels. Due to an absorption by the entrance window and the charge loss effect in Si detectors, quantum efficiency drops to ~40% at 5 keV. The structure just above Cd/Te edge at 26.7 and 31.8 keV is from the Cd/Te fluorescence events detected in only Si layers. This structure and the other fluorescence/Compton events are seen as non-diagonal components in the line spread function (see Fig. 3).
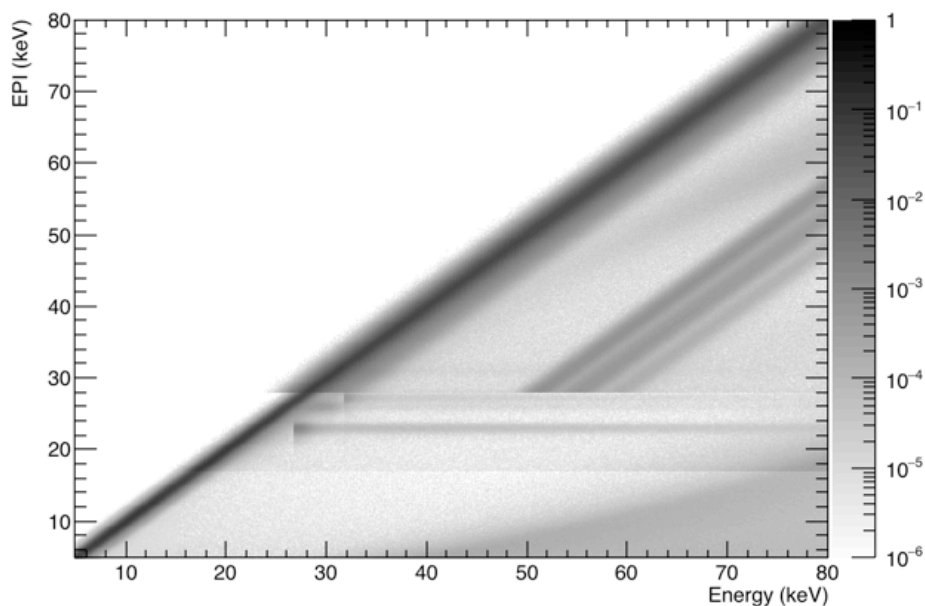

Fig. 3. Line spread function for all layers of HXI2.

2.4 Comparison with previous releases

First release.

2.5 Final remarks

N/A

3 Release CALDB 20160920

Filename	Valid date	Release date	CALDB Versions	Comments
ah_hx1_lsf_20140101v002.fits	2015-01-01	2016-09-20	004	ah_hx1_lsf_20160720v001.fits
ah_hx1_qe_20140101v002.fits	2015-01-01	2016-09-20	004	ah_hx1_qe_20160720v001.fits

.

| ah_hx2_lsf_20140101v002fits | 2015-01-01 | 2016-09-20 | 004 | ah_hx2_lsf_20160720v001fits |
| ah_hx2_qe_20140101v002.fits | 2015-01-01 | 2016-09-20 | 004 | ah_hx2_qe_20160720v001.fits |

3.1 Data Description

The observational data of Crab nebula listed in Table 2 are used for checking the response validity.

Table 2. The list of data used for checking response validity

OBS ID	Start date	Target	Net exposure (HXI1 / HXI2)
100044010	2016-03-25 12:35:48	Crab nebula	5.9 ks / 6.1 ks

3.2 Data Analysis

The observed data of Crab nebula are fitted with a simple power-law model by the 'canned' RMF (ah_hxi_rmf_20151115v001.fits) and the ARF prepared for the pre-launch scientific simulations. The spectra, models and ratio between these are plotted in Fig. 4. The ratios of both HXI1 and HXI2 show a large discrepancy between the models and data below ~10 keV.
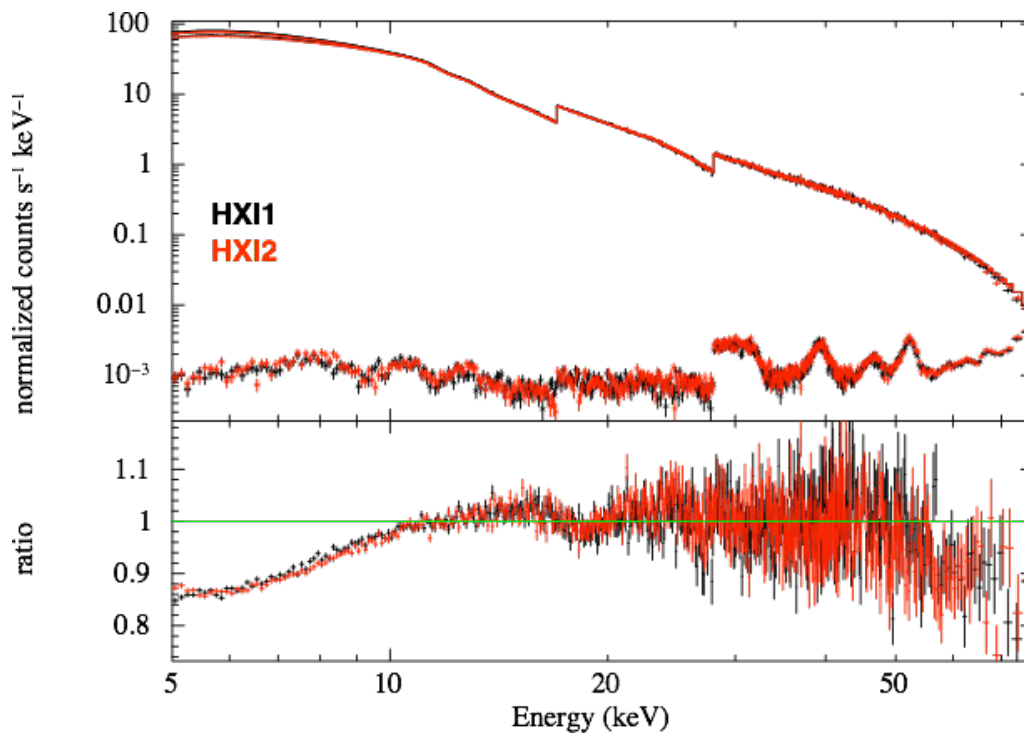

Fig. 4. Crab spectra, power-law models and the ratios between these.

For solving this problem, following changes are applied to the LSF/QE files:

1. Consider digital thresholds applied in orbit
2. Use hxievtid to the event reconstruction of the simulated data
3. Add an absorption by 5-μ m-thick SiO_2 layers

The SiO_2 layer makes a large difference on the low energy response, while the effect from the first and second items is very small.

In addition to the modification of the detector response, the PI-layer selection criteria are also updated. The previous selection and the updated selection are listed in Table 3. These criteria are determined in order to optimize the detection sensitivity. A major difference between the previous and updated criteria is that the energy range using only Si top layer (Layer0) is reduced for dealing with the unexpectedly high background rate in Si top layer.

Table 3. A comparison between the previous PI-layer selection criteria and the updated one.

Layer	Previous criteria	New criteria
0	PI>=0 && PI<2048	PI>=0 && PI<300
1	PI>=170 && PI<2048	PI>=120 && PI<2048
2	PI>=170 && PI<2048	PI>=120 && PI<2048
3	PI>=170 && PI<2048	PI>=120 && PI<2048
4	PI>=280 && PI<2048	PI>=300 && PI<2048

3.3   Results

A comparison between the Crab spectra and the models with the updated RMF is shown in Fig. 5. As the result, ratios between the observed spectra and the models becomes almost unity. Deviations from unity in the ratios are less than 5%. For this plot, the RMF are generated by summing up the QE of each pixel with a weight proportional to the observed Crab image. Basically, this RMF should be almost same as the response generated by the standard process (hxirspeffimg). Again, the ray tracing code is not used here, the ARF file for the pre-launch scientific simulations are used. Please note that in this plot, the spectra are fitted with a broken power-law model instead of a simple power-law to reproduce the observed spectra.
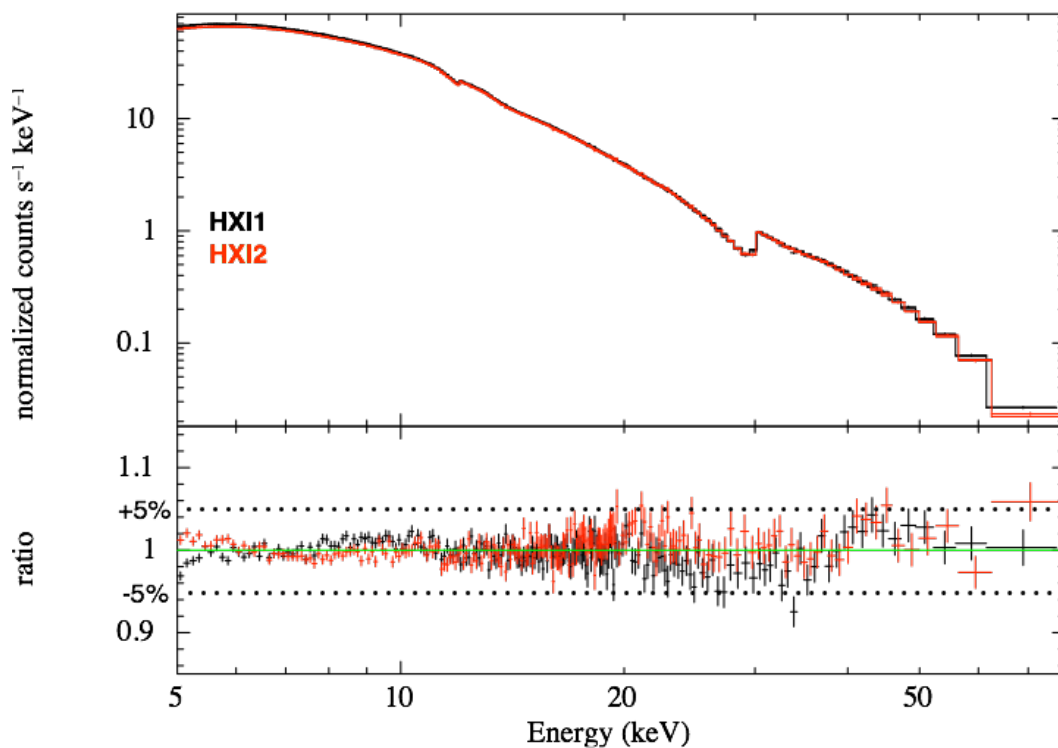
.

Fig. 5. Crab spectra and broken power-law models with a new RMF and PI-layer selection.
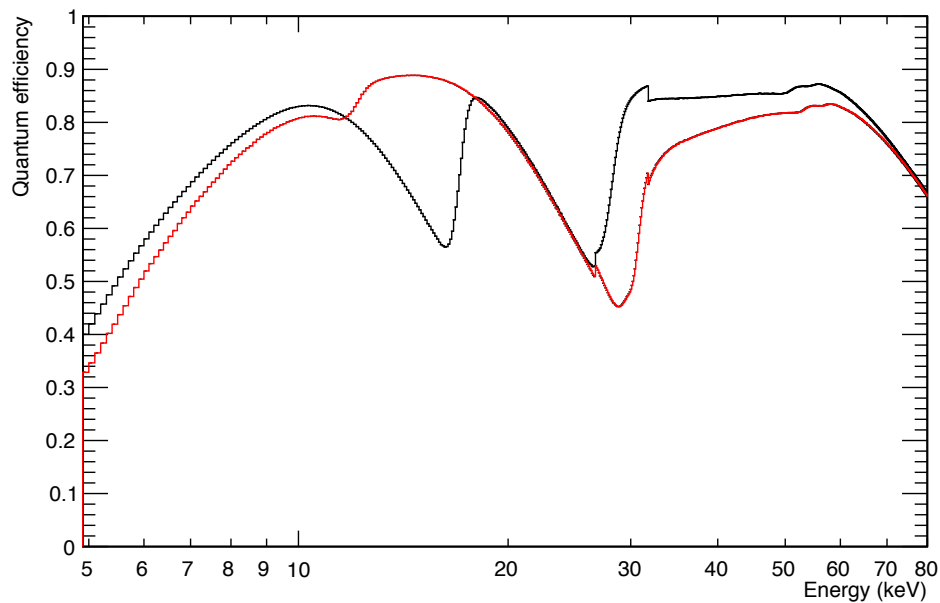
3.4 Comparison with previous releases

Fig. 6. Quantum efficiencies of HXI1 averaged over all the pixels. Black and red lines correspond the previous and the updated response, respectively.

A total detection efficiency of the updated response is shown in Fig. 6. In the lower energies, the efficiency decreases due to the SiO_2 layers on the surface of Si detectors. Dips at ~12 keV and ~30 keV are produced by the new PI-layer selection.

3.5   Final remarks

N/A